

# Surface Oxidation and Luminescence Properties of Weblike Agglomeration of Silicon Nanocrystals Produced by a Laser Vaporization–Controlled Condensation Technique

Shoutian Li, Stuart J. Silvers, and M. Samy El-Shall\*

Department of Chemistry, Virginia Commonwealth University, Richmond, Virginia 23284-2006

Received: October 17, 1996; In Final Form: January 2, 1997<sup>®</sup>

Weblike aggregates of coalesced Si nanocrystals are produced by a laser vaporization–controlled condensation technique. SEM micrographs show particles with  $\sim 10$  nm diameter but the Raman shift suggests the presence of particles as small as  $\sim 4$  nm. FTIR of the freshly prepared particles shows weak peaks due to the stretching, bending, and rocking vibrations of the Si–O–Si bonds, indicating the presence of a surface oxidized layer,  $\text{SiO}_x$  ( $x < 2$ ). Further oxidation of the Si core appears to be very slow and inefficient under ambient temperature, but annealing at higher temperatures facilitates the oxidation. The particles show luminescence properties that are similar to those of porous Si and Si nanoparticles produced by other techniques. The nanoparticles do not luminesce unless, by exposure to air, they acquire the  $\text{SiO}_x$  passivated coating. They show a short-lived blue emission characteristic of the  $\text{SiO}_2$  coating and a biexponential longer-lived red emission. The short lifetime component of the red emission, about  $12 \mu\text{s}$ , does not depend on emission wavelength. The longer-lived component has a lifetime that ranges from 80 to over  $130 \mu\text{s}$  (at 300 K), increasing with emission wavelength. The results are consistent with the quantum confinement mechanism as the source of the red photoluminescence.

## Introduction

In recent years, there has been an intense interest in the synthesis and characterization of nanoparticles.<sup>1–8</sup> Due to their finite small size, the nanoparticles often exhibit novel properties which are different from the bulk materials' properties.<sup>1–8</sup> Research in this area is motivated by the possibility of designing nanostructured materials that possess novel electronic, optical, magnetic, photochemical, and catalytic properties. Such materials are essential for technological advances in photonics, quantum electronics, nonlinear optics, and information storage and processing.

Among the many interesting nanoparticles, silicon nanocrystals show important promise for use in Si-based devices for optical communication. This exciting possibility has been hampered by the indirect band gap of bulk Si which prevents efficient electron–photon energy conversion. However, the discovery that porous and nanocrystalline Si emit visible light with a high quantum yield has raised hopes for new photonic Si-based devices.<sup>9–16</sup> This discovery has also stimulated interest in the synthesis of Si nanocrystals which are believed to be the luminescent centers in porous silicon.<sup>9,17–25</sup>

Various methods have been used to make Si nanocrystals. They have been generated by the slow combustion of silane,<sup>26</sup> reduction of  $\text{SiCl}_4$  by Na,<sup>27</sup> separation from porous Si,<sup>28</sup> UV or IR laser photolysis of silane-type precursors,<sup>29</sup> thermal evaporation,<sup>30</sup> microwave discharge,<sup>31</sup> RF sputtering,<sup>32</sup> and high-temperature aerosol techniques.<sup>18</sup> In most cases, some control over particle size can be achieved by lowering the concentration of the nucleating particles. Laser vaporization of metals has the advantage of eliminating the need for high temperatures and for chemical precursors. By coupling laser vaporization with controlled condensation from the supersaturated vapor, we are able to achieve good control over the particles' size and the aggregate state.<sup>33–38</sup> Furthermore, the use of mixtures of reactive/inert gases can control the chemical composition of the composite particles or the thickness and composition of passivated surface coating layers.

The structure, size distribution, morphology, and surface composition of the nanocrystals depend to a large extent on the method of preparation. Therefore, it is important to compare the physical and optical properties of Si nanocrystals prepared by different synthesis techniques. In this paper we describe the application of our new technique, laser vaporization–controlled condensation (LVCC),<sup>33–38</sup> for the synthesis of Si nanocrystals. We present a composite study of the morphology of the as-deposited particles, their surface oxidation, and their luminescence. The main focus of the paper is on the photoluminescence of the Si nanocrystals. However, an understanding of the mechanism of photoluminescence requires detailed information on the chemical composition, surface oxidation, and morphology of the Si particles. The ultimate goal of utilizing the Si nanoparticles in device applications also requires systematic studies of their surface oxidation and stability.

The outline of the paper is as follows. Our LVCC synthesis and the methods used to characterize the particles are described in the Experimental Section. The results are presented in five parts: (1) results pertaining to particle structure from SEM, Raman, and X-ray diffraction studies; (2) results of FTIR oxidation studies on particles annealed at different temperatures and produced under different oxygen pressures; (3) UV–visible absorption results from which the indirect band gap of the Si nanoparticles is estimated; (4) dispersed photoluminescence spectra using both cw and pulsed laser excitations; and (5) time-resolved photoluminescence decays obtained by monitoring luminescence at various wavelengths. Finally, the results are summarized and the mechanism of nanoparticle photoluminescence is discussed.

## Experimental Section

**Synthesis.** The Si nanoparticles used in these experiments were prepared in a modified, upward thermal diffusion cloud chamber by the LVCC method.<sup>38</sup> A sketch of the chamber with the relevant components necessary for the synthesis of nanoparticles is shown in Figure 1. The chamber consists of two horizontal, circular stainless steel plates, separated by a circular

<sup>®</sup> Abstract published in *Advance ACS Abstracts*, February 1, 1997.

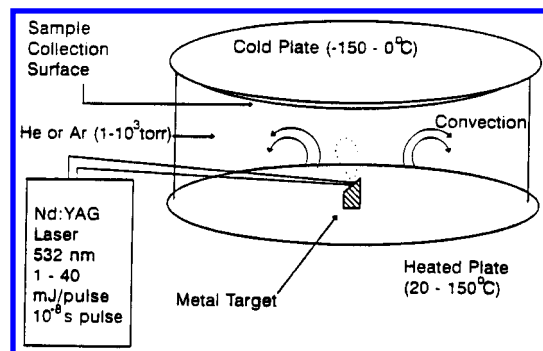


**Figure 1.** Experimental setup for the synthesis of the nanoparticles using laser vaporization in a convective atmosphere.

glass ring. A metal target of interest is set on the lower plate, and the chamber is filled with a pure carrier gas such as helium or Ar (99.99% pure) or a mixture containing a known composition of a reactant gas (e.g.  $O_2$  in case of oxides). The metal target and the lower plate are maintained at a temperature higher than that of the upper one (temperatures are controlled by circulating fluids). The top plate can be cooled to less than 150 K by circulating liquid nitrogen. The large temperature gradient between the bottom and top plates results in a steady convection current which can be enhanced by using a heavy carrier gas such as Ar under high-pressure conditions ( $10^3$  Torr).

The Si vapor is generated by pulsed laser vaporization using the second harmonic (532 nm) of a Nd:YAG laser (15–30 mJ/pulse,  $10^{-8}$  s pulse). The laser beam is moved on the Si surface in order to expose new surface to the beam and assure good reproducibility of the amount of Si vapor produced. Following the laser pulse, the ejection of the metal atoms and their eventual interaction with the ambient atmosphere will take place. Since the target surface where evaporation occurs is located near the middle of the chamber (about 0.5 reduced height) and the ambient temperature rapidly decreases near the top plate, it is likely that maximum supersaturation develops within the upper half of the chamber above the surface target (perhaps closer to the target than to the top plate). This supersaturation can be increased by increasing the temperature gradient between the target and the top plate. The higher the supersaturation, the smaller the size of the nucleus required for condensation. The role of convection in the experiments is to remove the small particles away from the nucleation zone (once condensed out of the vapor phase) before they can grow into larger particles. The rate of convection increases with the temperature gradient in the chamber. Therefore, by controlling the temperature gradient, the total pressure and the laser power (which determines the number density of the metal atoms released in the vapor phase), it is possible to control the size of the condensing particles.

Nichrome heater wires are wrapped around the glass ring and provide sufficient heat to prevent condensation on the ring and to maintain a constant temperature gradient between the metal target and the top plate. The particles formed in the nucleation zone condense on the top plate during the laser vaporization. In a typical run, the laser operates at 20 Hz for about 1–2 h. Then the chamber is brought to room temperature and the particles are collected under atmospheric conditions. Glass slides or metal wafers can be attached to the top plate when it is desired to examine the morphology of as-deposited particles. No particles are found on any other place in the chamber except on the top plate; this supports the assumption that nucleation takes place in the upper half of the chamber and that convection carries the particles to the top plate where deposition occurs.

## Structural Characterization

**X-ray Diffraction, Raman, and FTIR.** X-ray diffraction spectra are obtained on a Rigaku diffractometer equipped with a Cu  $K\alpha$  source. About 10 mg of the nanoparticles are pressed into a smooth layer on the surface of a metal holder.

The Raman spectra are obtained using an Ar ion laser (514.5 nm) for excitation coupled with a SPEX-1403, 0.85 m double spectrometer. A steel cone with an inner diameter of 0.15 cm is used to mount the nanoparticle sample at ambient temperature. The resolution of the spectrometer is better than  $1\text{ cm}^{-1}$  in the  $100\text{--}1000\text{ cm}^{-1}$  range.

FTIR spectra are obtained using a Perkin-Elmer 1600 FTIR in the range of  $400\text{--}4000\text{ cm}^{-1}$  with  $4\text{ cm}^{-1}$  resolution. The sample (about 0.2 mg) is ground and pressed into KBr pellets using a Fisher IR-pellet maker.

**Optical Spectroscopy.** The UV-vis spectra are obtained using a Shimadzu UV-265 spectrometer. A colloid solution of the Si nanoparticles in methanol is prepared ultrasonically and used in a quartz cuvette at room temperature.

The photoluminescence of Si nanoparticles is measured using both cw and pulsed lasers for excitation. In the CW excitation experiments a Spectra-Physics Model 2020 Ar ion laser is used for excitation (363.8 and 514.5 nm lines) and the luminescence is dispersed with a SPEX 1403 double monochromator, detected by a RCAC31034 photomultiplier and recorded with a computer. The S20 photocathode sensitivity cuts off just before 900 nm; the spectra are not corrected for the wavelength dependence of the detection system efficiency. The pulsed laser experiments use for excitations the frequency-doubled output (340.0 nm) of a Lambda-Physik LPD-3002 dye laser which is pumped by the 532 nm second harmonic of a Nd:YAG laser, and the 266 nm fourth harmonic of the YAG laser. The Si nanoparticles are pressed onto the surface of a KBr pellet and the laser light is directed onto the pellet. Luminescence from the sample is dispersed by a SPEX 1 m spectrometer fitted with an EMI 9558 photomultiplier (S20 photocathode). For dispersed luminescence spectra the photomultiplier output is processed by a PAR Model 162 boxcar averager and recorded by a computer. The spectra terminate at the spectrometer limit of 760 nm and, again, are not corrected for the wavelength dependence of the detection system efficiency. Time-resolved decays are averaged by a LeCroy 9450 oscilloscope and fit by a computer.

## Results

**I. Structure and Morphology.** The Si nanoparticles appear as a yellow powder. The SEM micrographs of the as-deposited particles on glass substrates reveal highly organized weblike structures characterized by micropores with wall thicknesses of 10–20 nm. The weblike morphology is similar to that of the silica nanoparticles prepared by the same method using  $O_2$ /Ar or  $O_2$ /He gas mixtures.<sup>37,38</sup> The weblike structure with strings of aggregated Si nanoparticles is shown in Figure 2. The individual particles are spherical and uniform in size, about 10 nm in diameter, and are connected in a weblike structure.

The Raman spectrum, displayed in Figure 3, shows a sharp peak at about  $510\text{ cm}^{-1}$ . This is close to the Raman allowed optical phonon characteristic of microcrystalline silicon at  $520\text{ cm}^{-1}$ .<sup>39</sup> The downshift of this band in our Si nanoparticles is attributed to size and strain effects.<sup>13,40,41</sup> We note that porous Si samples prepared under various etching conditions show Raman shifts which have been correlated to the Si particle size. For example, Raman shifts of 517, 515, 507, and  $501\text{ cm}^{-1}$  were correlated to particle sizes of 7, 4.8, 2.5, and  $\sim 1.6\text{ nm}$ , respectively.<sup>42</sup> Based on the Raman shift of our sample, the average particle size can be estimated as  $\sim 4\text{ nm}$ . This is

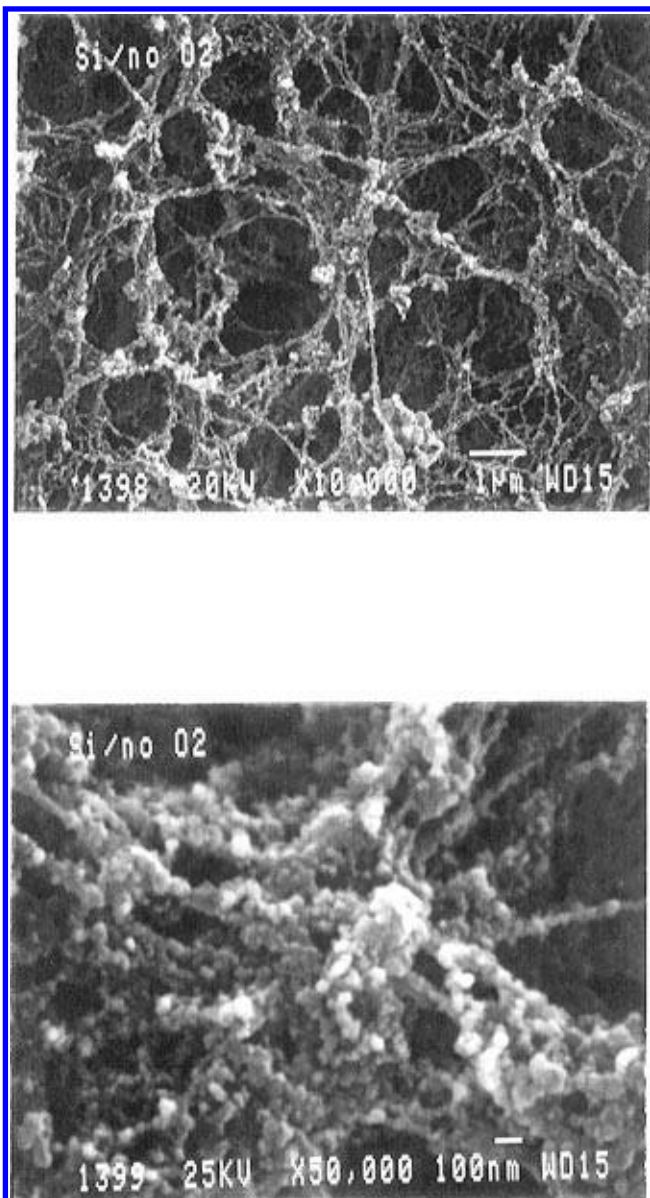


**Figure 2.** SEM micrographs of the weblike agglomeration of the surface-oxidized Si nanocrystals.

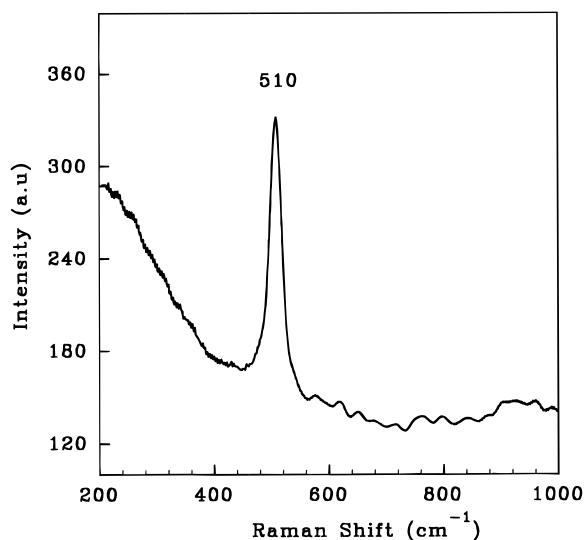


**Figure 3.** Raman spectrum of the surface-oxidized Si nanocrystals.

considerably smaller than the particle size shown by the SEM micrographs and this suggests that particles smaller than the SEM is able to detect may be present in our sample.

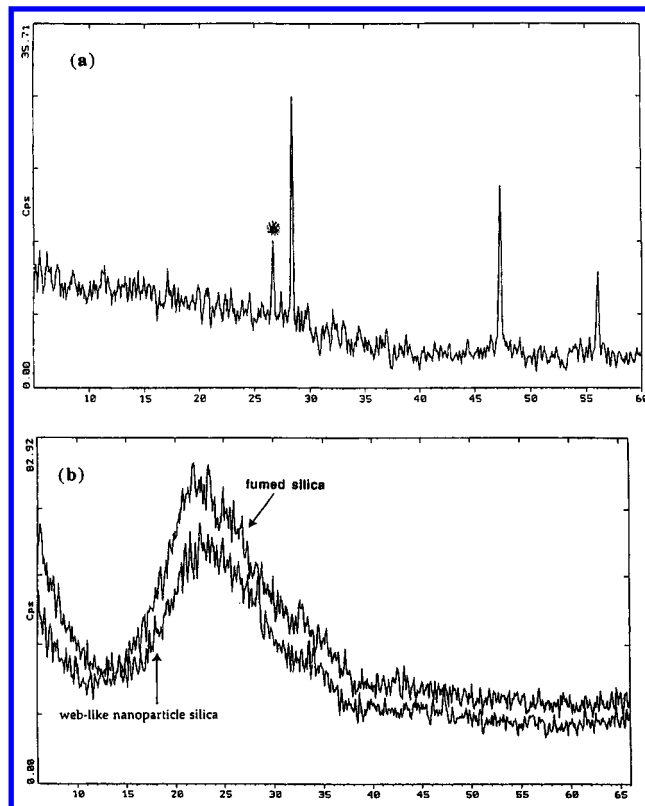


**Figure 4.** X-ray diffraction of (a) surface-oxidized Si nanocrystals (\* is due to the sample holder) and (b) silica nanoparticles.

The crystallinity of the particles is verified by the X-ray diffraction spectrum shown in Figure 4a. The spectrum conclusively shows crystalline Si lines 111, 220, and 311 at scattering angles of 28°, 47°, and 56°, respectively. Such crystalline lines are not present in the X-ray diffraction pattern of silica nanoparticles prepared in the presence of O<sub>2</sub>. These particles exhibit a completely amorphous structure similar to that of fumed silica as shown in Figure 4b.

**II. Surface Oxidation.** The surface oxidation of the Si nanoparticles is studied by FTIR. Figure 5 shows the dependence of the IR absorption spectrum on the annealing temperature of the nanoparticles. The spectra of the as-deposited particles (Figure 5a) are measured 20 min after removing the particles from the preparation chamber. Spectra b, c, d, e, and f are measured after annealing the as-deposited sample in air for 10 min at 288 °C, 60 min at 288 °C, 60 min at 427 °C, 10 min at 593 °C, and 60 min at 593 °C, respectively. The FTIR of the as-deposited sample (Figure 5a) shows a broad absorption band at about 1080 cm<sup>-1</sup> accompanied by weak bands at 958, 880, and 454 cm<sup>-1</sup>. The main band at 1080 cm<sup>-1</sup> is due to Si—O—Si stretching and is usually observed in thin films of amorphous silicon oxide (SiO<sub>x</sub> with *x* varying from 0 to 2).<sup>43,44</sup> Other peaks observed in the IR of amorphous SiO<sub>x</sub> films are a weak band at 800 cm<sup>-1</sup> and a moderate peak at 460 cm<sup>-1</sup> which are assigned to bending and rocking vibrations, respectively, of the Si—O—Si bonds.<sup>44</sup> In addition, a shoulder at 956 cm<sup>-1</sup> is also observed and attributed to the stretching of the Si—O—Si bridge.<sup>45,46</sup> Another peak at 880 cm<sup>-1</sup> has also been observed in the IR of amorphous silicon films<sup>43</sup> and is also observed in our sample. The origin of this peak has not been clearly identified. Previous studies have attributed this feature to various sources: (1) to a Si<sub>2</sub>O<sub>3</sub> phase within the amorphous Si film;<sup>47</sup> (2) to the combination of Si—(O<sub>2</sub>Si<sub>2</sub>), Si—(O<sub>3</sub>Si), and Si—(O<sub>4</sub>) structures;<sup>43</sup> (3) to the Si—N bond;<sup>48</sup> and to the motion of the nonbridging Si—O bonds or change in the Si—O—Si angle.<sup>49</sup> In addition, Knolle and Maxwell, from both experimental and theoretical analysis, assign the 880 cm<sup>-1</sup> peak to

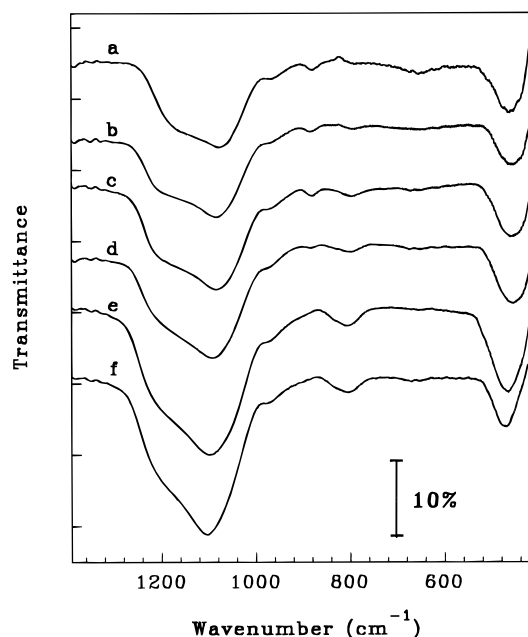


**Figure 5.** FTIR of Si nanocrystals: a, as-deposited particles; spectra b, c, d, e, and f are measured after annealing the as-deposited sample in air for 10 min at 288 °C, 60 min at 288 °C, 60 min at 427 °C, 10 min at 593 °C, and 60 min at 593 °C, respectively.

the interaction between Si and nonbridging O atoms in  $\text{SiO}_2$ .<sup>50</sup> This last explanation is best supported by our results, as explained below.

Comparing our results to previous ones on thin films of amorphous  $\text{SiO}_x$  films and nanoparticles,<sup>43–47</sup> we assign the observed IR peaks of the as-deposited Si sample to a surface oxide layer of  $\text{SiO}_x$  that apparently forms after the particles are removed from the reaction chamber. Annealing the particles for 10 min at 288 °C (Figure 5b) results in the appearance of a weak band at 800  $\text{cm}^{-1}$  and an increase in both the broad band at 1080  $\text{cm}^{-1}$  and the 460  $\text{cm}^{-1}$  band. These changes are attributed to developing the oxide layer ( $\text{SiO}_x$ ) by both increasing its oxygen content (i.e.,  $x$  increases toward 2) and increasing its thickness through the slow oxidation of the Si core. These changes are more apparent after annealing the particles for 60 min at 288 °C as shown in Figure 5c. It should be noted that no significant shift of the broad band at 1080  $\text{cm}^{-1}$  is observed even when the annealing time is increased to 90 min at 288 °C. However, after annealing the particles for 60 min at 427 °C, a noticeable decrease in the 880  $\text{cm}^{-1}$  band and a high-frequency shift of the main broad band to 1086  $\text{cm}^{-1}$  occur as seen in the spectrum of Figure 5d. These changes can clearly be produced by annealing the particles for only 10 min at 593 °C as shown in Figure 5e. In this case the weak band located at 880  $\text{cm}^{-1}$  disappears, the band at 800  $\text{cm}^{-1}$  increases, and the broad band shifts to 1094  $\text{cm}^{-1}$ . By continuously annealing the particles for 60 min at 593 °C, (spectrum 5f), little changes can be observed in the IR except the further shift of the broad band to 1106  $\text{cm}^{-1}$ . It should be noted that spectra e and f are very similar to the IR spectrum of silica nanoparticles prepared by using  $\text{O}_2/\text{Ar}$  gas mixture.<sup>37</sup> In particular, the band at 800  $\text{cm}^{-1}$  is very pronounced in the silica nanoparticles as is the broad band at 1100  $\text{cm}^{-1}$  which has the same frequency as in the spectra of Figure 5, e and f. This is taken as evidence for complete oxidation of the Si nanoparticles (including the core particles) achieved by annealing the particles at quite high temperatures such as 593 °C.

To further support the conclusion that the changes in the IR spectra are directly related to the oxidation of the Si nanoparticles, we prepared several Si samples by using variable amounts

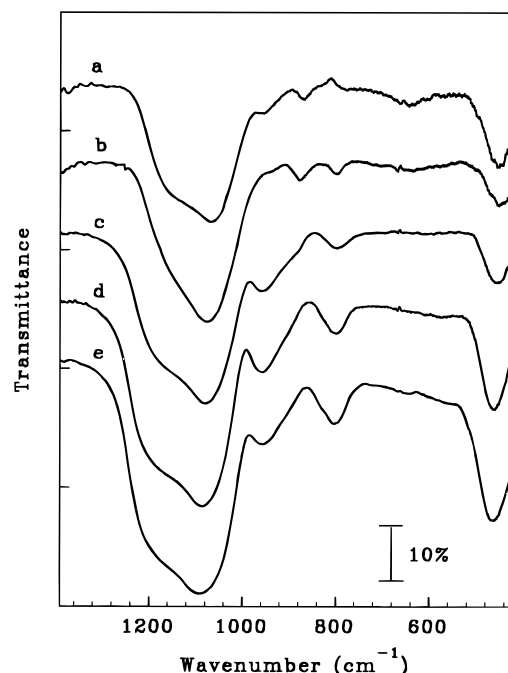


**Figure 6.** FTIR of oxidized Si nanoparticles; a, no  $\text{O}_2$  added during preparation, spectra b, c, d, and e are measured for particles prepared by adding 5, 20, 100, and 500 Torr of  $\text{O}_2$ , respectively, during preparation.

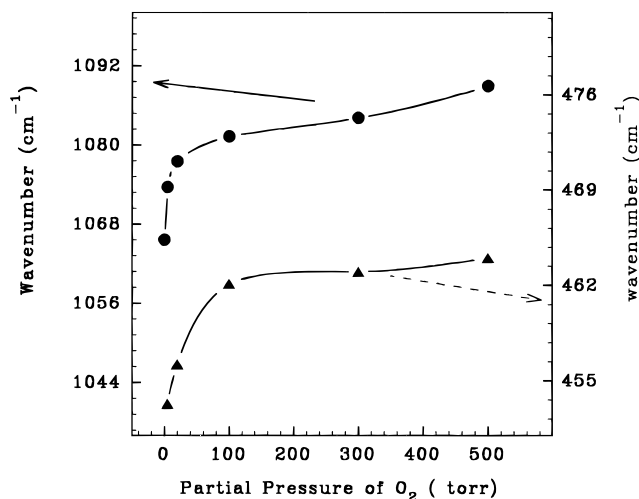


**Figure 7.** FTIR shifts of the 1080 and 460  $\text{cm}^{-1}$  bands as a function of  $\text{O}_2$  partial pressure during the particles' formation.

of  $\text{O}_2$  in the reaction chamber. The IR spectra of the as-deposited particles (measured within 20 min after removing the particles from the chamber) are shown in Figure 6. As the partial pressure of  $\text{O}_2$  increases in the reaction chamber, the following features can be observed in the IR spectra: (1) the broad band at  $\sim 1080 \text{ cm}^{-1}$  and the 460  $\text{cm}^{-1}$  band shift to higher frequency, (2) the shoulder peak at 956  $\text{cm}^{-1}$  becomes stronger, (3) the peak at 881  $\text{cm}^{-1}$  disappears, and (4) the weak peaks at 800 and 460  $\text{cm}^{-1}$  become stronger. Figure 7 illustrates the magnitude of the shift in the broad band at 1080  $\text{cm}^{-1}$  and in the 460  $\text{cm}^{-1}$  peak as a function of  $\text{O}_2$  partial pressure during the particles' formation. These peak shifts are strongly related to both the oxygen content and the thickness of the  $\text{SiO}_x$  oxide layer. It has been shown both experimentally and by theoretical analysis that the thicker the  $\text{SiO}_2$  oxidation layer or the higher the oxygen content of the  $\text{SiO}_x$  layer, the higher the frequency of the Si–O–Si stretching and rocking vibrations.<sup>43,44,51,52</sup> The disappearance of the 880  $\text{cm}^{-1}$  peak at higher  $\text{O}_2$  partial pressure (more than 20 Torr in our experiments) is consistent with the



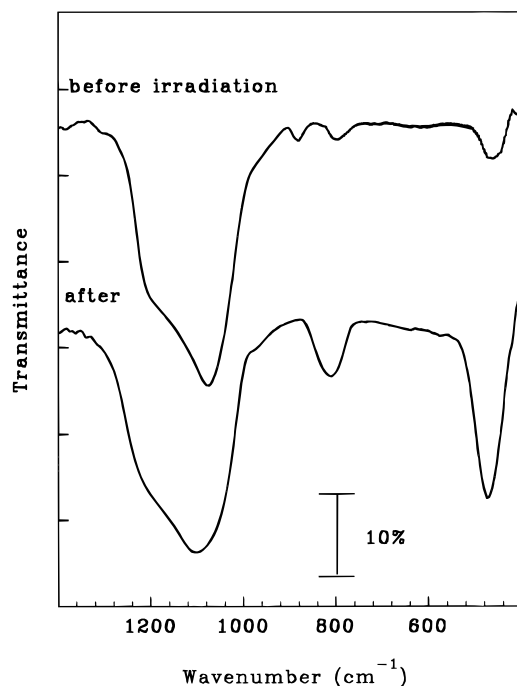


**Figure 8.** FTIR of the Si nanoparticles before and after irradiation with the 532 nm second harmonic of the Nd:YAG laser.

assignment of Knolle and Maxwell, who attributed this peak to the interaction between core Si and nonbridging O atoms in the SiO<sub>2</sub> layers.<sup>50</sup> Oxidation eliminates the nonbonding Si atoms and thus weakens the interaction between Si and nonbridging O atoms. Thus the 880 cm<sup>-1</sup> peak gradually decreases and eventually disappears at higher O<sub>2</sub> partial pressure or higher annealing temperatures.

Another result relating to the oxidation of the Si nanoparticles is that complete oxidation can be achieved by focusing the 532 nm second harmonic of the Nd:YAG laser (30 mJ/pulse) on the Si particles in air. Bright red orange luminescence is observed upon irradiation of the particles with a single laser pulse (10 ns). This is accompanied by a mild sound, and the yellow Si particles turn white.<sup>53</sup> The observed emission can be reproduced by irradiation of a fresh Si sample, but after the particles turn white, further irradiation does not produce any red emission. We measured the IR of the Si particles before and after the irradiation with the YAG laser and the results are shown in Figure 8. The IR spectrum measured after irradiation shows clearly all the features associated with complete oxidation of the Si nanoparticles. These features include the disappearance of the 880 cm<sup>-1</sup> peak, the enhancement of the 470 and 800 cm<sup>-1</sup> peaks, and the high-frequency shift and enhancement of the broad band at 1080 cm<sup>-1</sup>. These results indicate that the incident laser pulse efficiently breaks the thin SiO<sub>x</sub> layer around the Si core and, therefore, induces immediate oxidation of the bare particles in air.

The surface composition of the oxidized Si nanoparticles was also examined by X-ray photoelectron spectroscopy (XPS). Figure 9 shows the XPS spectrum of the particles prepared by using 2% O<sub>2</sub> in He as a reactive/carrier gas mixture. The spectrum shows two peaks at about 99.8 and 103 eV, which are assigned to the Si 2p photoelectrons of the unoxidized Si core and the SiO<sub>x</sub> oxide layer, respectively. This result agrees well with previous XPS studies of SiO<sub>2</sub> particles.<sup>44,54–56</sup>

From the FTIR and the XPS studies we conclude that the as-deposited Si nanoparticles are coated with a surface layer of SiO<sub>x</sub> when exposed to air. The oxygen content can be increased to approach  $x = 2$  by annealing the particles at lower temperatures (300 °C) in air. We estimate the thickness of the

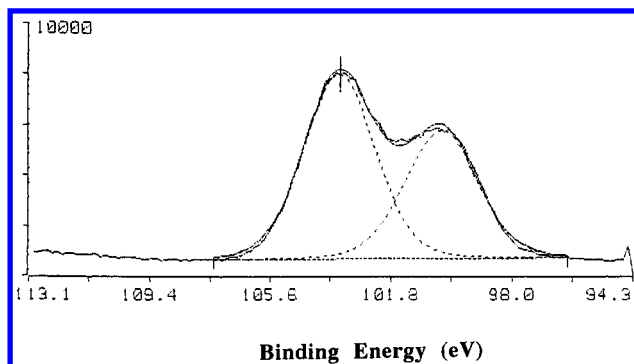


**Figure 9.** XPS spectra of the oxidized Si nanoparticles prepared using 2% O<sub>2</sub> in He.

SiO<sub>x</sub> layer (in the as-deposited particles) as 1–2 nm. The thickness of this layer can be increased by further oxidation of the core Si particles, which takes place efficiently only at relatively high temperatures (e.g., 10 min at 593 °C), or by rapid breaking of the oxide surface layer by, for example, irradiation with intense laser pulses. Under ambient temperature, further oxidation of the Si core appears to be very slow and inefficient. These conclusions are consistent with previous results which showed that the oxide growth rate of small Si particles is smaller than the rate of oxidation of Si wafers.<sup>57</sup> One explanation of this phenomenon is that stress in the oxide layer may suppress the oxidation of the small particles. Our results are also in full agreement with the conclusions of Hayashi et al. from their study of the surface oxidation of thermally evaporated Si nanoparticles (10 nm).<sup>44</sup>

**III. Optical Absorption.** Figure 10a shows the UV–vis absorbance of the Si nanoparticles suspended in methanol. The spectrum shows the absorption features associated with indirect band gap transitions, particularly the yellow absorption tail which extends from 400 nm across the visible and the stronger absorption from 370 to 240 nm. The indirect band gap of semiconductors can be obtained from the following relation<sup>58</sup>

$$(\alpha h\nu)^{1/2} = B(h\nu - E_g)$$

where  $\alpha$  is the reciprocal absorption length,  $h\nu$  is the photon energy,  $B$  is a constant, and  $E_g$  is the band gap. Using the yellow absorption tail in the UV–vis spectrum, we plot  $(\alpha h\nu)^{1/2}$  vs  $h\nu$  as shown in Figure 10b. The plot shows an approximate straight line which extrapolates to give 1.78 eV as the calculated band gap of the Si nanoparticles. This corresponds to 700 nm emission. The blue shift from the bulk Si indirect band gap (1.1 eV) is a direct manifestation of the quantum confinement effect.<sup>18,20,25</sup>

**IV. Photoluminescence Spectra.** The dispersed luminescence spectra of the Si nanoparticles excited by the 363.8 and 514.5 nm Ar ion cw laser lines are shown in Figure 11. In both spectra a broad emission is seen in the red region. This emission can be seen with the naked eye in the presence of normal room light. The luminescence quantum yield, estimated by using Rhodamine B as a relative standard, is about 1.3%. The red emission curve can be fit to a Gaussian shape. For the 363.8 nm excitation the width (fwhm) is 184 nm and the maximum is at 740 nm; for the 514.5 nm excitation the width is 190 nm and the maximum is at 760 nm. The 20 nm blue shift in the emission maximum for 363.8 nm excitation may arise as a result of excitation of higher energy states which are not accessible with longer wavelength excitations. With the quantum confinement interpretation,<sup>18,20,25</sup> this suggests that different sizes of nanocrystals are simultaneously present in our sample. Accordingly, the longer wavelength excitation selects

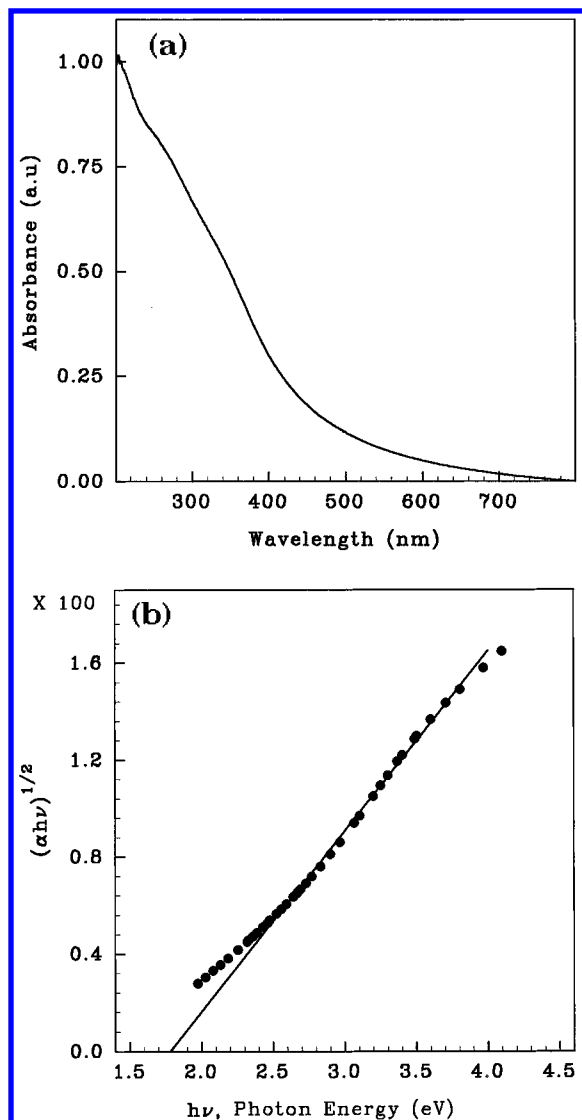


**Figure 10.** (a) UV-vis absorbance of Si nanocrystals suspended in methanol. (b) Plot of  $(\alpha h\nu)^{1/2}$  vs  $h\nu$  for the absorption tail of the Si nanocrystals.

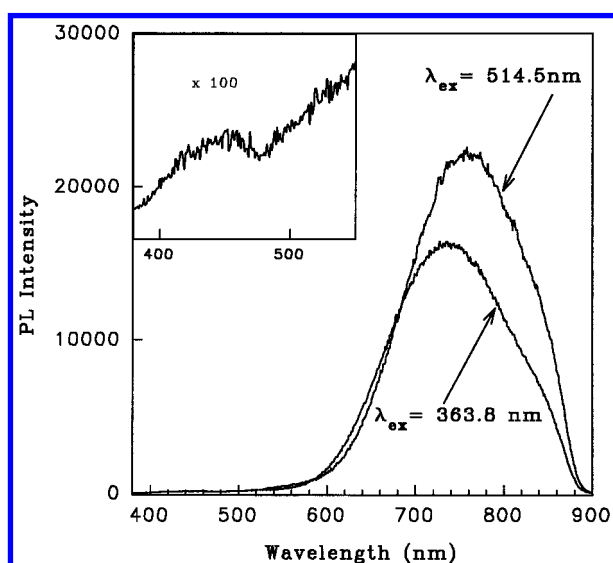


**Figure 11.** Dispersed emission of the Si nanocrystals excited by the 363.8 and 514.5 nm lines of the Ar ion laser.

larger particles which in turn emit further to the red than the smaller particles selected by the shorter wavelength excitation.

The inset in Figure 11 shows a weak blue emission feature that is observed when 363.8 nm excitation is used. This feature

peaks at 450 nm and appears similar to the blue emission observed when  $\text{SiO}_2$  nanoparticles are excited. This blue emission is more pronounced when pulsed excitation is used and will be discussed further below.

**V. Time-Resolved Photoluminescence.** Dispersed luminescence spectra obtained with 340 and 266 nm pulsed laser excitations are shown in Figure 12, a and b, respectively. It should be noted that the emission spectra terminate at the spectrometer limit of 760 nm and the spectra are not corrected for the wavelength dependence of the detection system efficiency. Therefore, the red emission bands actually peak at longer wavelengths than those shown in Figure 12a, and b. This detection limit should not affect the relative comparison of a series of spectra taken at different time delays or with different excitation energies. The spectra differ by the position of the boxcar gate, which ranges from 0  $\mu\text{s}$  delay with respect to the laser excitation pulse to 40  $\mu\text{s}$  delay. The 0  $\mu\text{s}$  delay spectrum enhances the blue emission component, since the lifetime associated with it is short (less than 20 ns) compared to the lifetimes of the red emission. The shape of the blue emission appears similar to that from  $\text{SiO}_2$  nanoparticles and it is probably due to the oxidized surface layer of the Si nanoparticles.<sup>37</sup> The CW excitation experiments, similar to time-integrated pulsed ones, weigh the long-lived red emission more heavily compared to the short-lived blue emission than do gated experiments with short delays. This makes the blue band hard to detect. By using the 266 nm excitation, the red emission shifts to shorter wavelength as compared to the emission from the 340 nm excitation. This again can be attributed to preferential excitation of the smaller Si particles by the 266 nm pulse.

As the boxcar delay increases, the blue emission decreases in intensity due to its relatively short lifetime and the red to blue intensity ratio increases. Also, the maximum of the red emission band shifts to longer wavelengths as the delay increases. This is due to the lifetime lengthening that occurs as emission wavelength increases. This lifetime lengthening can also be observed in the time- and frequency-resolved emission spectra. These decays are multiexponential but clearly have both long and short components. They can be fit to the biexponential form

$$I(t) = I_s^0 \exp(-t/\tau_s) + I_l^0 \exp(-t/\tau_l)$$

where the subscripts s and l refer to the short- and long-lived components respectively. A decay at 700 nm is shown in Figure 13 together with the biexponential fit. The short lifetime, about 12  $\mu\text{s}$ , does not depend on emission wavelength; the long lifetime ranges from 80 to over 130  $\mu\text{s}$ , increasing with emission wavelength. The dependence of  $\tau_l$  on emission energy is shown in Figure 14a, and the energy dependence of the intensity ratio,  $I_l^0/I_s^0$ , is shown in Figure 14b. The long lifetime and the intensity ratio increases with emission wavelength both contribute to the red shift with boxcar delay seen in the dispersed spectra (Figure 12).

## Discussion

The present study shows that weblike aggregates of coalesced Si nanocrystals, passivated by a  $\text{SiO}_x$  barrier layer exhibit intense red photoluminescence (PL) upon excitation with visible or UV light. The freshly prepared Si nanoparticles do not show the emission unless a passivated layer stabilizes the nanocrystal surface by saturating all the dangling bonds. FTIR of the freshly prepared sample shows weak peaks due to the stretching, bending, and rocking vibrations of the Si-O-Si bonds indicating the presence of the surface oxidized layer  $\text{SiO}_x$ , but no red or blue emission is observed until more complete development

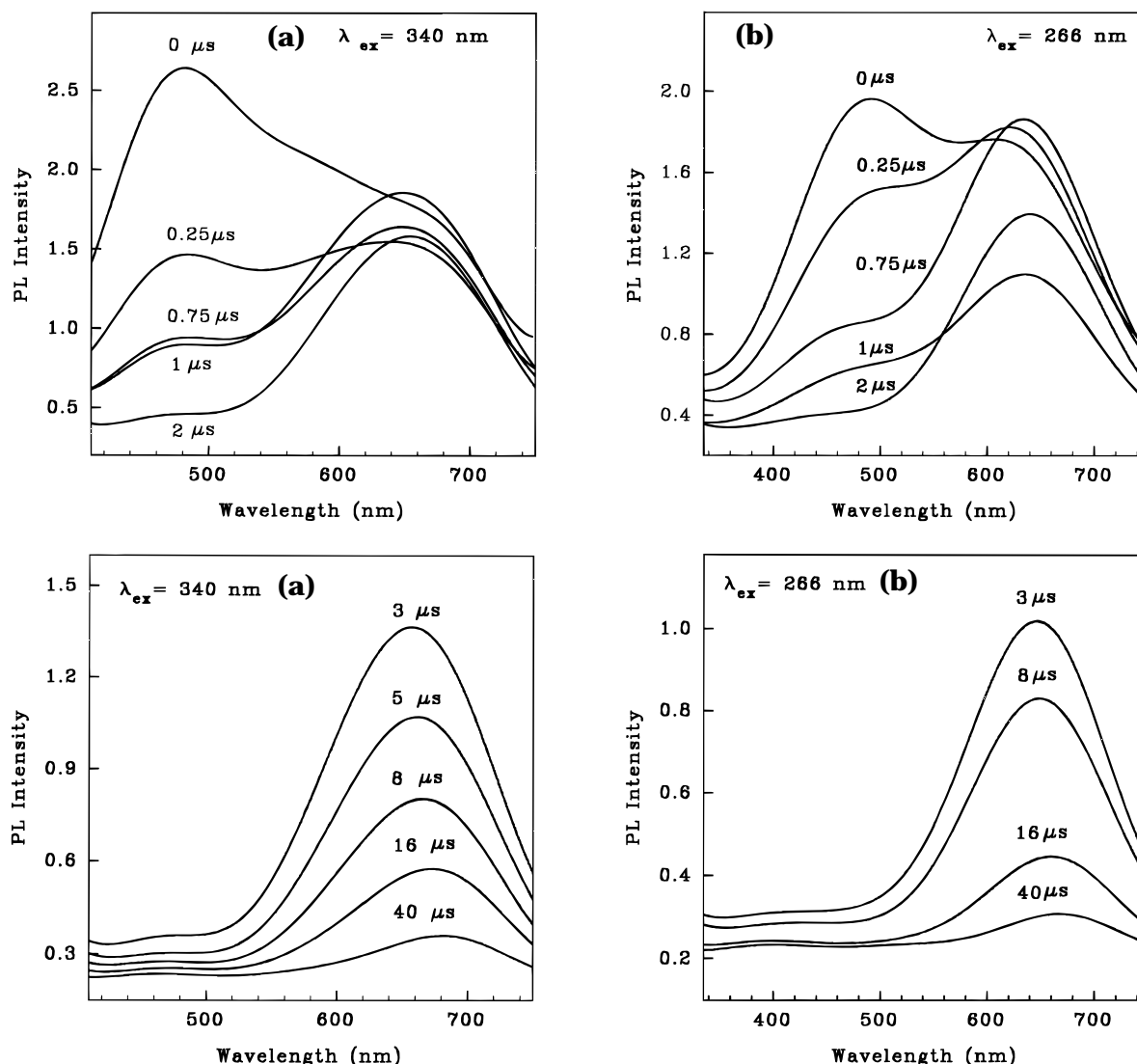


**Figure 12.** (a) Dispersed emission of the Si nanocrystals obtained with 340 nm pulsed laser excitation. (b) Dispersed emission of the Si nanocrystals obtained with 266 nm pulsed laser excitation.

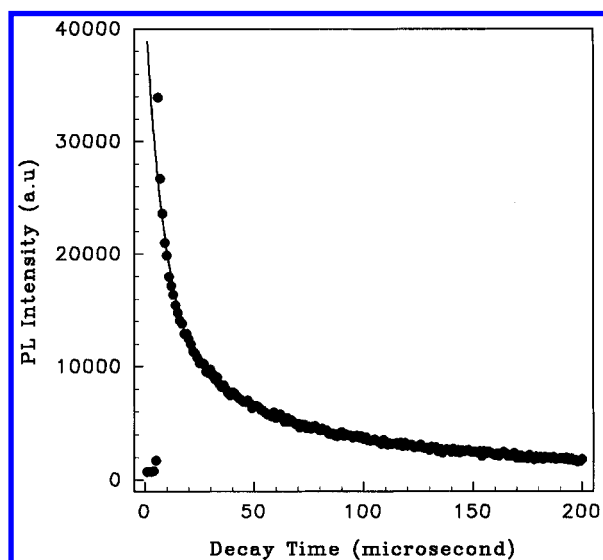


**Figure 13.** Decay of the PL from the Si nanocrystals at 700 nm (solid line represents the biexponential fit).

of the oxide layer has been achieved. This appears to be essential for efficient passivation of the nanocrystal surface. Part of this development appears to be the increase in the oxygen content of the oxide layer to approach the  $\text{SiO}_2$  composition; another part may be an increase in its thickness to form an

efficient barrier layer. This is apparently a slow process under normal ambient conditions since the emission can be observed only 1–2 days after the nanoparticles are removed from the reaction chamber to the ambient air. It is also important to note that fully oxidized Si nanoparticles with  $\text{SiO}_2$  composition and completely amorphous phase do not show the red PL upon UV or visible excitations.

The red PL from the Si particles shifts to longer wavelength with decreasing excitation energy. This emission is characterized by a multiexponential decay having a long component (80–130 ns at 300 K) that increases in lifetime and intensity with emission wavelength (630–740 nm). These features of the red emission are similar to those observed for porous  $\text{Si}^9-16$  and for Si nanocrystals.<sup>17-25</sup> Because of such strong similarity between the PL properties of porous Si and Si nanocrystals, Brus et al. concluded that the luminescing chromophore is the same in the two systems.<sup>18,20,25</sup> They assigned the red PL to single crystalline quantum confinement in which both electron and hole are in totally symmetric volume-confined states with no significant trapping within the optical absorption band gap.<sup>20,25</sup> The barriers to carrier mobility between crystallites make the radiationless processes much less important in nanocrystals. This results in weak PL efficiency in Si nanocrystals and porous Si.<sup>25</sup>

In addition to the red PL, we also observe a weak blue PL with pulsed laser excitation (266 and 340 nm). Its wavelength

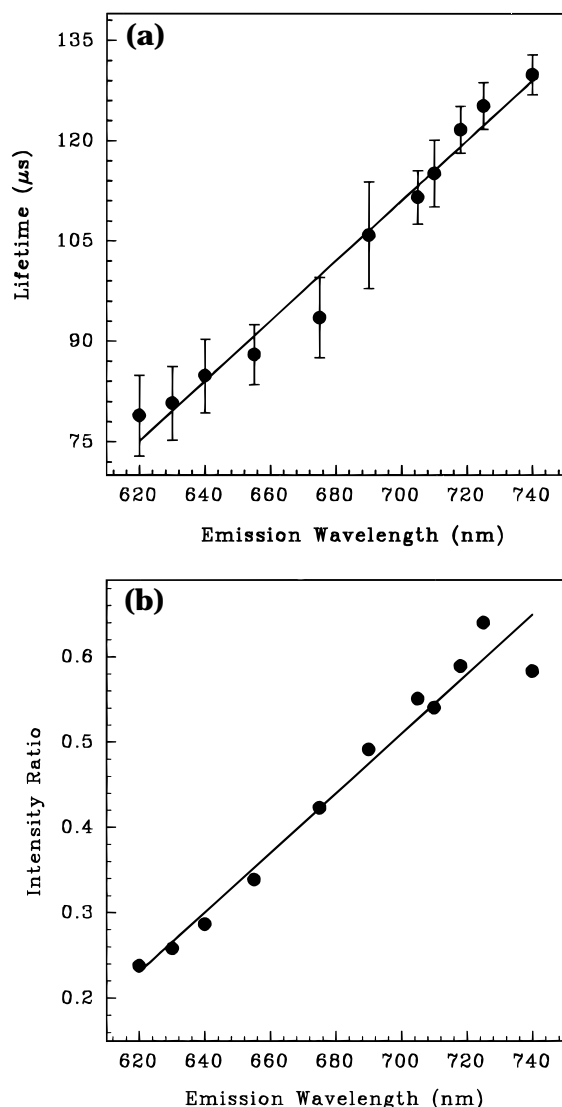


**Figure 14.** (a) Dependence of the lifetime of the longer-lived component of the red emission on the emission wavelength. (b) Dependence of the intensity ratio  $I_P/I_S$  on the emission wavelength.

does not shift with excitation wavelength and it can also be observed under high intensity CW 363 nm laser excitation. This blue emission has a fast decay (less than 20 ns) and it appears similar to the blue PL observed from amorphous silica ( $\text{SiO}_2$ ) nanoparticles.<sup>37</sup> Interestingly, there is no indication in Brus' papers that the fast decay blue PL has been observed from their Si nanocrystals.<sup>18,20,23,25</sup> However, the features we observe for the blue PL are similar to those reported by Kanemitsu using surface-oxidized Si crystallites prepared by laser breakdown of silane.<sup>21,22,24</sup> Kanemitsu also observed the slow decay red PL with very similar features to our present results and to those previously reported by Brus. However, in contrast to Brus, Kanemitsu proposed a model in which the red PL originates from surface localized states while the blue PL originates from the nanocrystal core.<sup>24</sup> According to this model, the shift of the red PL to longer wavelength with time delay is due to the relaxation of the carriers or excitons to lower energy states.

In comparing our results with those of Brus et al.<sup>18,20,25</sup> and Kanemitsu<sup>21,22,24</sup> on Si nanocrystals, it is important to point out the differences between the particles investigated in each study. The particles used by Brus and Kanemitsu were prepared by high-temperature pyrolysis and laser breakdown of disilane and silane, respectively. In both studies, the surface-oxidized Si crystallites were around 3 nm in diameter. In Brus' study, larger

crystallites with Si cores of  $>3$  nm and an oxidized layer of 0.5–1.0 nm emit in the 800–1000 nm range and smaller crystallites (with Si core diameters of 1–2 nm) emit in the 600–750 nm range. Our particles were prepared by laser vaporization of Si and the method does not involve hydrogen. As indicated by the FTIR, Raman, XPS, and X-ray diffraction data, our particles appear to be only a crystalline Si core coated with an oxide  $\text{SiO}_x$  layer. The SEM data indicates the presence of large particles ( $\sim 10$  nm) aggregated in a weblike morphology, while the Raman shift suggests an average particle size of  $\sim 4$  nm. If the estimation of the particle size from the Raman shift is reliable, a significant number of smaller particles ( $\sim 4$  nm) may exist in our sample to produce the observed red PL. The red PL from these aggregated solid particles at 300 K excited by 363.8 nm light shows a Gaussian-shaped band centered at  $\sim 740$  nm. The PL reported by Brus et al.<sup>25</sup> from 3 nm particles suspended in ethylene glycol glass at 15 K and excited by 350 nm shows a band centered at  $\sim 700$  nm as compared to 740 nm observed in our study. This shift in the PL may reflect larger size particles used in our experiments.

Simple three-dimensional quantum confinement calculations suggest the particle size must be less than 5 nm for visible emission. To be consistent with this, our sample must contain particles significantly smaller than the 10 nm ones indicated by the SEM data. The resolution of the SEM micrographs may be inadequate for the smaller particles or it may be that higher-level calculations that include electron–hole interactions are needed to give a better correlation between band gap and Si particle size.

In view of the many different mechanisms proposed to explain the visible PL from porous Si and Si nanocrystals,<sup>9–25</sup> we note that many of the observed features associated with the red PL from our particles can be explained by the quantum confinement mechanism. For example, the failure to observe the red PL from the freshly prepared particles and the long annealing time in ambient air required before emission can be observed can be explained by the need to provide an efficient surface passivation which permits radiative recombination in the crystallites by removing competitive nonradiative relaxation at the surface states. Also, the shift of the PL toward shorter wavelength by increasing excitation energy is explained by the selective excitation of the smaller particles which emit more to the blue. Finally, the increase in the lifetime of the longer-lived component of the red emission with emission wavelength is consistent with larger particles having longer lifetimes. In addition, we note that the features associated with the fast-decay blue emission cannot be explained with the confinement mechanism. For example, this emission does not shift with the excitation energy and its short lifetime does not depend on the emission wavelength. Moreover, this blue emission is similar to that observed from silica particles and several models related to surface defects and surface adsorbed OH groups have been proposed to explain it.<sup>37,59</sup>

The surprisingly long annealing time required in ambient air before efficient PL can be observed from the Si nanoparticles deserves further comment. This long passivation time may suggest that slow continuous oxidation of the Si core takes place in ambient air and this process results in a gradual decrease of the core size. Accordingly, the red PL is observed only when the size of the Si core becomes comparable to the quantum confinement regime. This suggestion appears to be consistent with the absence of red PL from the completely oxidized Si nanoparticles. To test the validity of this proposal, one must make systematic measurements of PL, Raman shift, and particle size over long particle oxidation times. If extended oxidation reduces the core size, one would expect to see a blue shift in



the red PL with also a significant peak narrowing as the Si core size continuously decreases. Such measurements are currently in progress in our lab.

## Conclusions

A method which combines laser vaporization of metal targets with controlled condensation in a diffusion cloud chamber is used to synthesize Si nanoparticles. The nanoparticles aggregate into a novel weblike porous microstructure. From the Raman shift of the Si nanoparticles, the average particle size is estimated as  $\sim 4$  nm. FTIR of the freshly prepared particles shows weak peaks due to the stretching, bending, and rocking vibrations of the Si—O—Si bonds, indicating the presence of a surface oxidized layer SiO<sub>x</sub> ( $x < 2$ ). Under ambient temperature, further oxidation of the Si core appears to be very slow and inefficient. Annealing at higher temperatures facilitates the oxidation.

The particles show luminescence properties that are similar to those of porous Si and Si nanoparticles produced by other techniques. The nanoparticles do not luminesce unless, by exposure to air, they acquire the SiO<sub>x</sub> passivated coating. They show a short-lived blue emission characteristic of the SiO<sub>2</sub> coating and a biexponential longer-lived red emission. The short lifetime component of the red emission, about 12  $\mu$ s, does not depend on emission wavelength. The longer-lived component has a lifetime that ranges from 80 to over 130  $\mu$ s (at 300 K), increasing with emission wavelength. The results are consistent with the quantum confinement mechanism as the source of the red photoluminescence.

**Acknowledgment.** The authors gratefully acknowledge financial support from the NASA Microgravity Materials Science Program (Grant NAG8-1276) and partial support from the National Science Foundation (Grant CHE 9311643). We thank Professor Jim Turner (VCU) for the Raman measurements and Dr. S. Ismat. Shah (E. I. du Pont Company, Wilmington, DE) for the XPS measurements.

## References and Notes

- (1) See for example: (a) *Nanomaterials: Synthesis, Properties and Applications*; Edelstein, A. S., Cammarata, R. C., Eds.; Institute of Physics Publishing: Bristol, U.K., 1996. (b) *Nanotechnology: Molecularly Designed Materials*; Chow, G. M., Gonsalves, K. E., Eds.; ACS Symposium Series 622; American Chemical Society: Washington, DC, 1996. (c) *Nanophase Materials: Synthesis, Properties, Applications*; Hadjiipanyis, G. C., Siegel, R. W., Eds.; Kluwer Academic Publications: London, 1994. (d) *Frontiers in Materials Science, Science* **1992**, 255, 1049. (e) Steigerwald, M. L.; Brus, L. E. *Acc. Chem. Res.* **1990**, 23, 183.
- (2) Alivisatos, A. P. *J. Phys. Chem.* **1996**, 100, 13226.
- (3) Siegel, R. W. *Nanostruct. Mater.* **1994**, 4, 121; *Annu. Rev. Mater. Sci.* **1991**, 21, 559.
- (4) Ahmadi, T. S.; Wang, Z. L.; Green, T. C.; Henglein, A.; El-Sayed, M. A. *Science* **1996**, 272, 1924.
- (5) Henglein, A. *J. Phys. Chem.* **1993**, 97, 5457.
- (6) Herron, N.; Calabrese, J. C.; Farret, W. E.; Wang, Y. *Science* **1993**, 259, 1426.
- (7) Ozin, G. A. *Adv. Mater.* **1992**, 4, 612.
- (8) Gleiter, H. *Adv. Mater.* **1992**, 4, 474.
- (9) Canham, L. T. *Appl. Phys. Lett.* **1990**, 57, 1046.
- (10) Cullis, A. G.; Canham, L. T. *Nature* **1991**, 353, 335.
- (11) *Light Emission from Silicon*; Iyer, S. S., Collins, R. T., Canham, L. T., Eds.; *Mater. Res. Soc. Proc.* **1992**, 256.
- (12) *Microcrystalline Semiconductors: Materials Science and Devices*; Fauchet, P. M., Tsai, C. C., Canham, L. T., Shimizu, I., Aoyahi, Y., Eds.; *Mater. Res. Soc. Proc.* **1992**, 283.
- (13) Sui S.; Leong, P. P.; Herman, I. P.; Higashi, G. S.; Temkin, H. *Appl. Phys. Lett.* **1992**, 60, 2086.
- (14) Cullis, A. G.; Canham, L. T.; Williams, G. M.; Smith, P. W.; Dosser, O. D. *J. Appl. Phys.* **1994**, 75, 493.
- (15) Canham, L. T.; Cullis, A. G.; Pickering, C.; Dosser, O. D.; Cox, T. I.; Lynch, T. P. *Nature* **1994**, 368, 133.
- (16) Chin, R. P.; Shen, Y. R.; Petrova-Koch, V. *Science* **1995**, 270, 776.
- (17) Brus, L. E. *Nature* **1991**, 353, 301.
- (18) Littau, K. A.; Szajowski, P. J.; Muller, A. J.; Kortan, A. R.; Brus, L. E. *J. Phys. Chem.* **1993**, 97, 1224.
- (19) Takagi, H.; Ogawa, H.; Yamazaki, Y.; Ishizaki, A.; Nakagiri, T. *Appl. Phys. Lett.* **1992**, 256, 117.
- (20) Wilson, W. L.; Szajowski, P. F.; Brus, L. E. *Science* **1993**, 262, 1242.
- (21) Kanemitsu, Y.; Ogawa, T.; Shiraishi, K.; Takeda, K. *Phys. Rev. B* **1993**, 48, 4883.
- (22) Kanemitsu, Y. *Phys. Rev. B* **1993**, 48, 12357.
- (23) Brus, L. J. *J. Phys. Chem.* **1994**, 98, 3575.
- (24) Kanemitsu, Y. *Phys. Rev. B* **1994**, 49, 16845.
- (25) Brus, L. J.; Szajowski, P. F.; Wilson, W. L.; Harris, T. D.; Schuppler, S.; Citrin, P. H. *J. Am. Chem. Soc.* **1995**, 117, 2915.
- (26) Fojtik, A.; Weller, H.; Fiechter, S.; Henglein, A. *Chem. Phys. Lett.* **1987**, 134, 477.
- (27) Heath, J. R. *Science* **1992**, 258, 1131.
- (28) Heinrich, J.; Curtis, C.; Credo, G.; Kavanagh, K.; Sailor, M. *Science* **1992**, 255, 66.
- (29) Cannon, W. R.; Danforth, S. C.; Flint, J. H.; Haggerty, J. S.; Marra, R. A. *J. Am. Ceram. Soc.* **1982**, 65, 324.
- (30) Matsunawa, A.; Katayama, S.; Arata, Y. *J. High Temp. Soc.* **1987**, 13, 69.
- (31) Takagi, H.; Yamazaki, Y.; Ishizaki, A.; Nakagiri, T. *Appl. Phys. Lett.* **1990**, 56, 2379.
- (32) Furukawa, S.; Miyasato, T. *Jpn. J. Appl. Phys.* **1988**, 27, 2207.
- (33) El-Shall, M. S.; Slack, W.; Vann, W.; Kane, D.; Hanley, D. *J. Phys. Chem.* **1994**, 98, 3067.
- (34) El-Shall, M. S.; Slack, W.; Hanley, D.; Kane, D. In *Molecularly Designed Ultrafine/Nanostructured Materials*; Gonsalves, K. E., Chow, G., Xiao, T. D., Cammarata, R. C., Eds.; Mater. Res. Soc. Proc., Materials Research Society: Pittsburgh, PA, 1994; Vol. 351, p 369.
- (35) El-Shall, M. S.; Graiver, D.; Pernisz, U.; Baraton, M. I. *Nanostruct. Mater.* **1995**, 6, 297.
- (36) Baraton, M. I.; El-Shall, M. S. *Nanostruct. Mater.* **1995**, 6, 301.
- (37) El-Shall, M. S.; Li, S.; Turkki, T.; Graiver, D.; Pernisz, U. C.; Baraton, M. E. *J. Phys. Chem.* **1995**, 99, 17805. El-Shall, M. S.; Graiver, D.; Pernisz, U. C. *Silica Nanoparticles*, US patent #5580655 issued on 12/03/1996.
- (38) El-Shall, M. S.; Li, S.; Graiver, D.; Pernisz, U. C. In ref 1b, Chapter 5, pp 79–99.
- (39) Okada, T.; Iwaki, T.; Yamamoto, K.; Kasahara, H.; Abe, K. *Solid State Comm.* **1984**, 49(8), 809.
- (40) Tsu, R.; Shen, H.; Dutta, M. *Appl. Phys. Lett.* **1992**, 60, 1112.
- (41) Kaneko, K.; Onisawa, M.; Kita, Y.; Minemura, T. *Jpn. J. Appl. Phys.* **1993**, 32, 4907.
- (42) Prokes, S. M. in Ref. 1-a, pp. 349–457; Prokes, S. M. *Bull. Am. Phys. Soc.* **1993**, 38, 157.
- (43) Nakamura, M.; Mochizuki; Usami, K. *Solid State Commun.* **1984**, 50(12), 1079.
- (44) Hayashi, S.; Tanimoto, S.; Yamanoto, K. *J. Appl. Phys.* **1990**, 68, 5300.
- (45) Koropecki, R. R.; Arce, R. *J. Appl. Phys.* **1986**, 60, 1802.
- (46) Lucovsky, G.; Yang, J.; Chao, S. S.; Tyler, J. E.; Czubatyi, W. *Phys. Rev. B* **1983**, 28, 3225.
- (47) Ritter, E. *Opt. Acta* **1962**, 19, 197.
- (48) Anderson, D. A.; Modell, G.; Paesler, M. A.; Paul, W. *J. Vac. Sci. Technol.* **1979**, 16, 906.
- (49) Shabalov, A. L.; Feldman, M. S. *Thin Solid Films* **1983**, 110, 215.
- (50) Knolle, W. R.; Maxwell, H. R., Jr.; Beneson, R. E. *J. Appl. Phys.* **1980**, 51, 4385.
- (51) Boyd, I. W.; Wilson, J. I. B. *J. Appl. Phys.* **1987**, 62, 3195.
- (52) Boyd, I. W. *Appl. Phys. Lett.* **1987**, 51, 418.
- (53) El-Shall, M. S.; Graiver, D.; Pernisz, U. C. *Silicon Nanoparticles* US patent application #DC 4304, filed 11/22/1995.
- (54) Finster, J.; Schulze, D.; Meisel, A. *Surf. Sci.* **1985**, 162, 671.
- (55) Feldman, A.; Sun, Y. N.; Farabaugh, E. F. *J. Appl. Phys.* **1988**, 63, 2149.
- (56) Bell, F. G.; Ley, L. *Phys. Rev. B* **1988**, 37, 8383.
- (57) Okada, R.; Iijima, S. *Appl. Phys. Lett.* **1991**, 58, 1662.
- (58) Hagfeldt, A.; Gratzel, M. *Chem. Rev.* **1995**, 95, 49.
- (59) Tamura, H.; Ruckschloss, M.; Wirschem, T.; Veprek, S. *Appl. Phys. Lett.* **1994**, 65, 1537. Morisaki, H.; Hashimoto, H.; Ping, F. W.; Nozawa, H.; Ono, H. *J. Appl. Phys.* **1993**, 74, 2977.